

On the Origin of GW190425

Nicholas Farrow

Supervisors:
Xingjiang Zhu
Eric Thrane

An honours thesis presented for the degree of
Bachelor of Science (Honours)



School of Physics and Astronomy
Faculty of Science
Monash University
Australia

2019

Abstract

The LIGO/Virgo collaborations have recently announced the detection of GW190425, the second gravitational wave observation from a double neutron star merger. The total mass of the binary is significantly higher than any previously measured double neutron star at $3.4_{-0.1}^{+0.3}M_{\odot}$, possibly indicating the existence of a new population. We propose that GW190425 may have formed via unstable case BB mass transfer, where the progenitor $\sim 4 - 5M_{\odot}$ helium star and neutron star binary experienced a common envelope event that brought the binary to a short < 1 hr orbital period. Subsequent supernova of the helium star formed a heavy $2M_{\odot}$ neutron star, likely in a significantly eccentric orbit. Using recently developed posterior reweighting methods, we constrain the eccentricity of GW190425 at 10 Hz to be $e \leq 0.007$ with 90% confidence. We simulate unstable case BB binaries and find that their orbits circularise to $e \lesssim 10^{-4}$ by the time they reach the Advanced LIGO/Virgo frequency band. While we are currently unable to determine whether GW190425 formed via this scenario, future detectors which can observe at lower frequencies may be able to measure significant eccentricities of double neutron star inspirals and distinguish their formation scenarios.

Acknowledgements

I would like to thank my supervisors Xingjiang Zhu and Eric Thrane. Xingjiang provided me with research opportunities that I had not dreamt I would be able to experience during an undergraduate science degree, and I thank him dearly for his encouragement and assistance. Thank you to Eric for his awe-inspiring discussions, guidance, patience in explanations, and invitations for me to work closely with the gravitational wave community. Thank you to Isobel Romero-Shaw who has provided vital technical assistance throughout the year, and allowed me access to her code. My family, friends, and especially Alicia, have provided me unfaltering support and understanding of my study commitments. Finally I would like to thank my fellow honours students and I wish them all success in their future endeavours.

Contents

Abstract	1
Acknowledgements	2
Contents	3
List of Figures	4
1 Introduction	5
1.1 Eccentricity of Binary Inspirals	6
2 DNS Formation Channels	8
2.1 Dynamical Formation	8
2.2 Isolated Binary Evolution	9
2.2.1 Case BB Mass Transfer	9
2.2.2 Supernova kicks	11
2.3 Merger Rates	11
2.4 GW190425	13
3 Method	14
3.1 Searching for Eccentricity in GW190425	14
3.1.1 Fiducial Inference	14
3.1.2 Reweighting with Eccentricity	15
3.2 Supernova-induced Eccentricity Distribution	18
4 Discussion	21
4.1 GW190425 & Simulated Eccentricity Distributions	21
4.2 Future Eccentric Waveform Models	21
4.3 Future Detection	22
5 Conclusion	24
A Appendix	25
References	27

List of Figures

2.1	Illustration of unstable case BB mass transfer leading to a DNS merger. Credit: Carl Knox (unpublished).	10
2.2	Contour map of orbital eccentricity in radial-tangential velocity space. A kick to an initially circular binary ($0, \pm 1$) would likely introduce a significant radial velocity component that gives the binary an eccentric orbit. The boundary of velocity magnitude $\sqrt{2}$ represents the escape velocity, whereafter $e > 1$. Reproduced from Chaurasia & Bailes (2005).	12
3.1	Reweighting example for a single posterior sample with parameters Λ . Top: log-likelihoods of eccentric waveforms $\ln(\mathcal{L}(D \Lambda))$. Bottom: the cumulative likelihood function (CLF), $p(\Lambda D) < e$	16
3.2	A) SEOBNRE waveform generation times, B) Maximum overlap, C) Overlap calculation time. Mean of all 2×10^4 reweighted samples, plotted against eccentricity. Error bars are one standard deviation.	17
3.3	Fiducial (turquoise) and reweighted (grey) posterior distributions for GW190425. Intrinsic parameters chirp mass \mathcal{M} , mass ratio q , effective aligned spin χ_{eff} , and log eccentricity $\log_{10}(e)$ are plotted on the left. Extrinsic parameters luminosity distance d_L , binary inclination angle θ_{jn} , polarisation angle ψ , and orbital phase ϕ are plotted on the right.	18
3.4	Top Right: Maxwell-Boltzmann kick velocity distributions for large kicks (265 km s^{-1}) in pink, small kicks (30 km s^{-1}) in blue. Bottom Right: Semimajor axes distributions before and after supernovae for simulated DNS; initial log-uniform semimajor axis distribution shown by red line. Left: Eccentricity distributions immediately after supernovae.	19
3.5	Simulated eccentricity distributions for large (dashed) and small (dotted) kick velocity distributions under binary assumptions for GW190425; compared to the recovered eccentricity distribution from GW190425. All distributions are shown at a mean gravitational wave frequency of 10 Hz.	20
4.1	Simulated eccentricity distributions for large (dashed) and small (dotted) kick velocity distributions at 5 mHz, which will be within the frequency band of future detector LISA.	22
A.1	The \log_{10} orbital periods of unstable case BB mass transfer DNS as simulated by Vigna-Gómez et al. (2018) (Figure 8) using COMPAS. The periods are approximately log-uniformly distributed between 0.1 – 1 hr. Purple diamonds represent Galactic DNS. Color denotes the number of cores within the common envelope phase: orange for a double-core common envelope, red for a single core, and blue for no cores.	26

Chapter 1

Introduction

On the 25th of April 2019, Advanced LIGO/Virgo made the second detection of gravitational waves (GW) originating from a double neutron star (DNS) inspiral ([The LSC and Virgo, 2019](#)). GW190425 is particularly interesting for several reasons. The total mass of GW190425 has been inferred to be $3.4_{-0.1}^{+0.3} M_{\odot}$, which is significantly larger than the observed Galactic DNS population. Out of the 18 known Galactic DNS only 17 have mass measurements, of which the most massive binary has a total mass of $2.875 \pm 0.0014 M_{\odot}$. Only 10 of the observed Galactic DNS will merge in a Hubble time and the total mass of GW190425 is inconsistent with this population at a 5σ level ([The LSC and Virgo, 2019](#)).

Secondly, the component spins for GW190425 are considerably high with a 90% credible region on χ_{eff} in the range $[0.008, 0.011]$, which is possibly higher than the fastest-spinning Galactic DNS J1946+2052 ([The LSC and Virgo, 2019](#); [Stovall et al., 2018](#)). This spin is higher than those predicted for a Galactic DNS at merger ([Zhu et al., 2018](#)), though it must be noted that zero-spin can not be ruled out for the event ([The LSC and Virgo, 2019](#)). The combination of these two unanticipated features of this event raises questions of what astrophysical processes led to this DNS merger; of most interest is the formation channel for GW190425.

Unlike the first DNS merger detection GW170817, the GW190425 signal was a single-detector event as it was only deemed significant in the Livingston detector of Advanced LIGO. Though, the signal was later found in the Virgo detector at a low significance with a signal-to-noise ratio of 2.5, this data was later used in parameter estimation. The false alarm rate for the signal was one in 6.9×10^4 years. The sky localisation for the detection was $\gtrsim 235$ times less precise than GW170817 and an alert was sent ~ 43 minutes after detection. No significant multimessenger counterparts, such as gamma-ray bursts, to GW190425 have been observed to date possibly due to the broad sky-localisation for the event ([The LSC and Virgo, 2019](#)).

As the merger rate implied by GW170817 is in tension with the merger rates predicted by numerical & n-body simulations, previously it has been conjectured that GW170817 may have been a statistical coincidence where the single detection provided an overestimation on the merger rate ([Belczynski et al., 2018](#); [Chruslinska et al., 2017](#)). However now with the detection of a second DNS merger this is unlikely, and the observational merger rate has increased to $1090_{-800}^{+1720} \text{ Gpc}^{-3} \text{ yr}^{-1}$ (from $800_{-680}^{+1970} \text{ Gpc}^{-3} \text{ yr}^{-1}$ in [Abbott et al. \(2019\)](#)), highlighting a need for a greater understanding of how these binaries form ([The LSC and Virgo, 2019](#)).

There are two predominant formation scenarios for compact binaries, which not only includes the formation of DNS but also binary black holes (BBH) and neutron star-black hole binaries (NS-BH). In the *dynamic formation* scenario, two compact objects form individually in a dense stellar environment such as a globular cluster, and the two compact objects are later brought together via dynamical interactions to form a binary. There are numerous subchannels for how these dynamic interactions take place, including gravitational wave captures around super-massive black holes ([O’Leary et al., 2009](#)), the formation of triples ([Antonini et al., 2017](#); [Rodriguez et al., 2018b,a](#)), and captures in dense stellar environments ([Banerjee, 2017a](#); [Samsing et al., 2019](#)). However, the dynamical formation process favours the formation of more massive binaries and thus tends to form BBH rather than DNS ([Banerjee, 2017b](#)).

Isolated binary evolution is thought to be the main channel for DNS formation. It involves an isolated field binary which undergoes a series of mass transfer stages and supernovae, as well as a common envelope where the two stars are contained within a slow rotating cloud of gas (Sparks & Stecher, 1974; Paczynski, 1976; Dewi et al., 2002; Beniamini & Piran, 2016; Tauris et al., 2017; Vigna-Gómez et al., 2018).

In the era of gravitational wave astronomy, inferring the parameters of these merging binaries may provide clues to their formation history. For instance, the mass distribution of merging binaries likely differs between formation channels and may allow us to distinguish between them (Schwab et al., 2010; Stevenson et al., 2015). The spin of each star in a binary can also inform us of its formation history. An isolated binary is likely to form with spins aligned to its orbital angular momentum (Boss, 1988), whereas dynamically formed binaries may have isotropic spins (Rodriguez et al., 2016; Stevenson et al., 2017).

The orbital eccentricity e , is a source parameter which has excellent potential to distinguish between formation scenarios. Eccentric binaries circularise as they evolve due to the emission of gravitational radiation (Peters, 1964), and as a result it is expected that the orbits of DNS that form as isolated binaries will become circular by the time they are detected by Advanced LIGO/Virgo. Hence, the observation of a gravitational wave with significant eccentricity ($e \gtrsim 0.1$) would provide strong evidence that the binary formed dynamically.

While the total mass of GW190425 is inconsistent with the Galactic DNS population, the component masses are consistent with the overall population of neutron stars (including those not in binaries). The more massive neutron star of GW190425 was measured at $1.61 - 2.47 M_{\odot}$, where the maximum mass for a single non-rotating neutron star has been found to be $2.0_{-0.1}^{+0.1} M_{\odot} \leq M_{\text{NS}} \leq 2.6_{-0.1}^{+0.1} M_{\odot}$ at 90% confidence (Alsing et al., 2018). It is challenging to explain the high mass of this system through standard isolated evolution, since the formation of these massive neutron stars are accompanied by large supernova kicks that are expected to disrupt binaries (Michaely et al., 2016). As the dynamical formation scenario is less restrictive on neutron star mass than the more delicate isolated evolution scenario, the high total mass of GW190425 could be explained through dynamical formation.

While the dynamical formation scenario can aptly explain the high mass of GW190425, the implied merger rate from GW190425 is far greater than the expected dynamical DNS merger rate (Bae et al., 2014; Belczynski et al., 2018). Hence, in this Thesis we propose how such a massive DNS could have formed via isolated binary evolution that involves an *unstable case BB mass transfer* stage. To evaluate this scenario we recover the eccentricity of GW190425, by following the work of Romero-Shaw et al. (2019) who have recently shown that all of the events in the first Gravitational-Wave Transient Catalogue (GWTC-1) of LIGO & Virgo have eccentricities consistent with zero. We also simulate unstable case BB mass transfer DNS with parameters similar to those of GW190425 for comparison.

We begin this Thesis with a description of orbital eccentricity and how it relates to gravitational waves in Section 1.1. In Chapter 2 we discuss the two predominant formation channels for DNS formation - dynamic and isolated evolution - followed by an explanation of how the supernova explosions that form NS can create eccentric binaries in Section 2.2.2. In Section 2.3 we discuss the contribution of each formation scenario towards the total DNS merger rate. Section 2.4 proposes how GW190425 may have formed via unstable case BB mass transfer as an isolated binary.

In Chapter 3 we first estimate the parameters that describe the GW190425 gravitational wave signal using Bayesian inference, and likelihood reweighting method to measure the eccentricity of the binary in Section 3.1. In Section 3.2 we present the expected eccentricities of DNS formed via unstable case BB mass transfer, and compare them to the recovered eccentricity of GW190425. Finally, in Chapter 4 we discuss our findings as to whether GW190425 is in-fact an unstable case BB mass transfer binary, as well as prospects and challenges in using eccentricity to identify these DNS populations with the next generation of gravitational wave detectors.

1.1 Eccentricity of Binary Inspirals

Eccentricity is an intrinsic parameter of a binary which describes the ellipticity of the orbit. An eccentricity $e = 0$ corresponds to a circular orbit, and as $e \rightarrow 1$ the orbit becomes increasingly elongated.

As gravitational systems lose energy from the emission of gravitational radiation, the semimajor axis and eccentricity of a binary decay over time (Peters, 1964). This leads to an *inspiral*, where the two compact objects become closer over time in an increasingly circular orbit. As the semimajor axis of the orbit decreases, the orbital velocities increase and consequently the orbital period of the two compact objects decreases which is reflected in the gravitational waves as an increasing frequency. The crescendo of this orbital frequency is reflected in the gravitational wave frequency as a *chirp*. This chirp ends with a *merger* between the two compact objects, forming a supramassive neutron star or a black hole which may momentarily *ringdown* and continue to emit gravitational waves. Peters (1964) provides an expression that calculates the semimajor axis of the binary at a given eccentricity

$$a(e) = \frac{c_0 e^{12/19}}{(1 - e^2)} \left[1 + \frac{121}{304} e^2 \right]^{\frac{870}{2299}} \quad (1.1)$$

where c_0 is found by solving the initial conditions of the binary $a(e_0) = a_0$.

As eccentricity decreases with time, it is a convention to state the eccentricity of a gravitational wave signal at a mean wave frequency of 10 Hz. Hence, it is useful to have an equation that relates a change in gravitational wave frequency to the shift in eccentricity (derived in Appendix A)

$$\frac{f(e)}{f_0(e_0)} = \left(\frac{\beta(e_0)}{\beta(e)} \right)^{3/2} \quad \text{where } \beta(e) = \frac{e^{12/19}}{(1 - e^2)} \left[1 + \frac{121}{304} e^2 \right]^{\frac{870}{2299}}. \quad (1.2)$$

Equation 1.2 is useful when we have an eccentricity e_0 at an initial reference frequency f_0 which we wish to shift to another reference frequency f , e.g. the conventional 10 Hz. But as it is difficult to find an inverse for $\beta(e)$, we use numerical root-finding methods to find the value for e that solves

$$g(e) = \frac{f}{f_0} - \left(\frac{\beta(e_0)}{\beta(e)} \right)^{3/2} = 0 \quad (1.3)$$

The eccentricity of a binary inspiral is imprinted onto the gravitational wave signal detected by Advanced LIGO/Virgo. A greater amount of gravitational energy is released when the two compact objects of an eccentric binary are closest, compared to the energy released when they are farther apart, modulating the gravitational wave signal. Eccentricity is currently not included in the waveforms used in current template-based gravitational wave searches at Advanced LIGO and Advanced Virgo (Abbott et al., 2019). Computationally efficient and complete inspiral-merger-ringdown eccentric waveform models are not currently available. The current quasi-circular waveform templates employed at these detectors have been shown to be capable of detecting slightly eccentric waveforms $e < 0.1$, but are ineffective at detecting binaries with higher eccentricities (Brown & Zimmerman, 2010). Using the inspiral-only `EccentricFD` waveform approximant, Lower et al. (2018) determined that the current generation of gravitational wave detectors will be sensitive to eccentricities $e \gtrsim 0.05$ at 10 Hz for GW150914-like events, showing that Advanced LIGO/Virgo will be able to distinguish these signals from instrumental noise. Past interferometer data has been revisited with waveform templates comprising of an eccentric inspiral waveform stitched with a quasi-circular merger template, but no new gravitational wave events were discovered (The LSC and Virgo & Salemi, 2019). Romero-Shaw et al. (2019), whose method we follow in this work, revisited GWTC-1 with a newly developed likelihood reweighting scheme for including higher order modes in gravitational wave inference (Payne et al., 2019). Romero-Shaw et al. (2019) find upper limits on eccentricity for all GWTC-1 events of 0.02 to 0.05 with 90% confidence.

Chapter 2

DNS Formation Channels

The formation scenario for DNS systems is a topic of contention as it is difficult to explain how two large stars are able to form compact objects in a tight enough orbit to merge within the age of the universe as a result of gravitational radiation. (Mandel & Farmer, 2018).

It should be noted that while we focus here on presenting the formation scenarios for DNS, the same scenarios apply to BBH as well as NS-BH binaries.

2.1 Dynamical Formation

The dynamic meeting scenario involves the merger of two compact objects which did not form in the same binary, but rather formed independently and were later brought together through interactions in dense stellar environments. Within the dynamical formation scenario there are several subchannels including gravitational wave captures around supermassive black holes (O’Leary et al., 2009), isolated and globular cluster triples (Antonini et al., 2017; Rodriguez et al., 2018b,a), and captures in dense stellar environments (Banerjee, 2017a,b; Samsing et al., 2019).

In dense regions, such as globular clusters or star clusters, interactions between massive objects are common and lead to behaviour such as mass segregation where heavier objects, generally black holes, sink towards the centre of the cluster (Sigurdsson & Hernquist, 1993; Zwart & McMillan, 2000). Single neutron stars can pair up with other neutron stars within the globular cluster core, forming DNS with short merger times (Zevin et al., 2019). As this channel involves neutron stars forming separately from each other, there is reduced constraint on parameters such as mass when compared to other formation channels.

Binaries which form through dynamical interactions can have a wide range of eccentricities at 10 Hz, as these systems can merge quickly enough such that they retain eccentric orbits before they circularise due to the emission of gravitational waves. As we will see in Section 3.2, binaries that form through the isolated binary evolution channel will completely circularise before 10 Hz, hence an observation of a significantly eccentric $e \gtrsim 0.1$ gravitational wave is a strong indicator of dynamical formation.

Rodriguez et al. (2018b,a) simulated N-body interactions in globular clusters where three- and four-body encounters led to about half of BBH mergers within a cluster, where $\sim 10\%$ of these mergers had significant eccentricities $e \gtrsim 0.1$ at 10 Hz. However this does not necessarily carry over to DNS systems as the N-body simulations conducted by Banerjee (2017b) found that energy injection by black holes will inhibit two-body interactions of less massive objects, meaning that neutron stars are prevented from effectively participating in exchange interactions where a neutron star in a binary is often replaced by an intruding black hole. Dynamic encounters of isolated field triples may form highly eccentric binaries $(1 - e) \lesssim 10^{-6}$ at 10 Hz (Antonini et al., 2017), but again this is primarily thought to occur with BBH for the aforementioned reason.

Antonini & Perets (2012) studied the evolution of binaries in the environment of supermassive black holes at the galactic center. Kozai-Lidov oscillations occur in these triples, comprised of an inner binary and outer supermassive black hole, in which the eccentricity and inclination of the DNS binary can significantly change in a periodic manner (Kozai, 1962; Lidov, 1962). Antonini & Perets

(2012) found that $\sim 10\%$ of these DNS have eccentricities of $e > 0.1$ at 10 Hz, about 0.5% have eccentricities larger than 0.5, and $\sim 0.1\%$ have very large eccentricities $e \approx 1$. Though, these events were found to be rare with ~ 1 per 10 Myr per Milky-Way-like Galaxy, as we will see in Section 2.3.

2.2 Isolated Binary Evolution

It is generally considered that isolated binary evolution is the dominant channel in DNS formation, responsible for at least 14 of the known Galactic DNS (Vigna-Gómez et al., 2018). Isolated binary evolution begins with two orbiting zero age main sequence (ZAMS) stars, where one of the stars begins to grow in size as it transitions out of its hydrogen fusion phase. The larger star may overflow its *Roche lobe*, the volume in which matter is gravitationally bound to the star, resulting in mass being accreted onto the smaller star. This mass transfer continues until the hydrogen envelope of the larger star is stripped off, leaving a helium star (He star) also known as a Wolf-Rayet star. Sometime later this He star undergoes a supernova, collapsing into a neutron star.

After some time the secondary star also begins to exit its main sequence, where it grows in stellar radius and overflows its Roche lobe. This interaction is dynamically unstable and the hydrogen is stripped off the secondary star into a common envelope where now a neutron star and He core are engulfed in a cloud of hydrogen (Paczynski, 1976). Dynamical friction is imposed on the two nuclei, decreasing their orbital velocities and bringing them closer together with a shorter orbital period (Sparks & Stecher, 1974; Dewi et al., 2002; Vigna-Gómez et al., 2018). Angular momentum is transferred from the binary onto the surrounding envelope causing it to decrease in density, potentially resulting in the ejection of the hydrogen envelope (Tauris et al., 2017).

The resulting system is a tightly bound neutron star and He star binary. Depending on the conditions, the binary may undergo a series of mass transfer stages. For example, *case A* mass transfer occurs while the hydrogen core is still burning, whereas if the helium core is burning when the mass transfer is initiated then it is known as *case BA* (see e.g. Dewi & Pols (2003)). *Case BB* mass transfer occurs if the helium core has finished burning but before the ignition of carbon (Dewi et al., 2002; Dewi & Pols, 2003). Here we will focus on case BB mass transfer which is of particular interest for attempting to explain GW190425.

2.2.1 Case BB Mass Transfer

Case BB transfer can be stable or unstable. Stable case BB mass transfer occurs when the He star overflows its Roche lobe as a stable flow of almost pure helium onto the companion neutron star (Delgado & Thomas, 1981; Dewi et al., 2002). Mass is transferred from the He star and is accreted onto the neutron star, also increasing its angular momentum, causing the *recycled* neutron star to spin up (Tauris et al., 2017).

Unstable case BB mass transfer, illustrated in Figure 2.1, occurs when the companion to the neutron star is a high-mass He-rich giant (Panel A) (Belczynski et al., 2002). Helium is pulled from the helium star at a rate faster than it can be accreted onto the neutron star, creating a helium common envelope that surrounds the neutron star and a carbon-oxygen core (Panel C) (Belczynski et al., 2002). Angular momentum is transferred from the neutron star and carbon-oxygen core to the surrounding medium, which can eject the helium envelope leaving a tight neutron star CO core binary (Panel D). Using population synthesis code COMPAS, Vigna-Gómez et al. (2018) found that these unstable case BB mass transfer binaries achieve orbital periods approximately log-uniformly distributed between 0.1 – 1 hr (Figure A.1 in Appendix).

The resulting binary is tight enough for it to likely survive the supernova of the carbon-oxygen core (Panel E). As the carbon-oxygen core has been stripped of its helium envelope, it is expected that the final supernova in an unstable case BB binary will be an ultra-stripped supernova. It may be possible for these binaries to inspiral with significant eccentricities acquired from the supernova kick (Vigna-Gómez et al., 2018) (see Section 2.2.2).

Ivanova et al. (2003) simulated the stellar evolution of 60 He-NS binaries with helium star masses between $2.5 - 6M_{\odot}$ with a $1.4M_{\odot}$ NS, finding that all binaries throughout this mass range can experience a common envelope, but this depends on the orbital period at the time when mass transfer

initiates. They found that these common envelope binaries can form DNS with merger timescales < 10 Myr, consistent with the findings of [Belczynski et al. \(2002\)](#). The simulations by [Ivanova et al. \(2003\)](#) also show that a heavy He-NS binary can survive the common envelope in an unstable case BB mass transfer, with one of the simulated binaries retaining a $3.01M_{\odot}$ helium star post-common envelope.

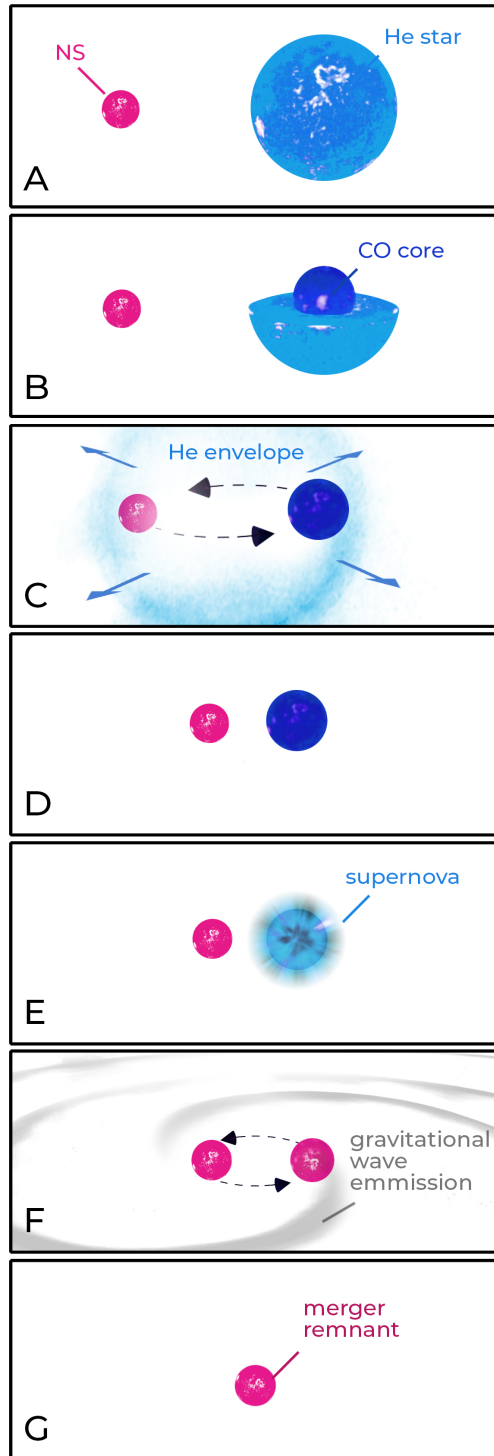


Figure 2.1: Illustration of unstable case BB mass transfer leading to a DNS merger. Credit: Carl Knox (unpublished).

2.2.2 Supernova kicks

For decades it has been noticed that neutron stars have velocities much greater than their progenitors (e.g. [Gunn & Ostriker \(1970\)](#)). When a star undergoes a supernova, the asymmetric distribution of mass during the collapse gives the neutron star a kick. These kicks are presumed to provide neutron stars with their high velocities. The distribution of kick velocity magnitudes is often described by a Maxwell-Boltzmann distribution, where the three degrees of freedom corresponds to three-dimensional space. The magnitude of this kick depends on the type of supernova, where core collapse supernovae (CCSN) are thought to produce large kicks with Maxwellian dispersion $\sigma_v = 265 \text{ km s}^{-1}$ ([Hobbs et al., 2005](#); [Hansen & Phinney, 1997](#)). Another supernovae type is ultra-stripped supernovae (USSN) which are thought occur in case BB mass transfer binaries as a result of the removal of hydrogen and helium envelopes, leaving an ultra-stripped core that undergoes iron core collapse with an extremely fast explosion ([Tauris et al., 2013, 2015](#)). Electron capture supernovae (ECSN) occur as a result of inverse β -processes which remove free electrons from the star, causing a reduced electron degeneracy pressure that allows the star to collapse ([Rakavy et al., 1967](#); [Finzi & Wolf, 1967](#)). Both ECSN and USSN are thought to produce small kicks with Maxwellian dispersion $\sigma_v \approx 30 \text{ km s}^{-1}$ (see, e.g. [Podsiadlowski et al. \(2004\)](#) for ECSN, and [Pfahl et al. \(2002\)](#) for USSN). Supernova kicks are thought to disrupt many binaries, providing the star with an orbital velocity greater than its escape velocity. Binaries which are not unbound by the kick are likely to acquire significant orbital eccentricity, as demonstrated by the vast non-zero eccentricity area in [Figure 2.2](#) (reproduced from [Chaurasia & Bailes \(2005\)](#)).

Following [Brandt & Podsiadlowski \(1995\)](#) we define the dimensionless mass of the binary

$$\tilde{m} = \frac{m_1 + m_2}{m'_1 + m_2} \quad (2.1)$$

where m_1 and m_2 are the masses of the progenitor binary, m'_1 is the mass of the star post supernova. We also define dimensionless kick velocity \tilde{v} as

$$\tilde{v} = \frac{v_{\text{kick}}}{v_{\text{orbit}}} \quad (2.2)$$

The resultant orbital eccentricity after the supernova is

$$e = \left[1 - \tilde{m} \left(2 - \tilde{m} \left(1 + 2\tilde{v} \cos \phi \cos \theta + \tilde{v}^2 \right) \right) \right. \\ \left. \times \left((1 + \tilde{v} \cos \phi \cos \theta)^2 + (\tilde{v} \sin \theta)^2 \right) \right]^{\frac{1}{2}}, \quad (2.3)$$

where ϕ is the angle between the direction of the star's velocity vector and the kick vector, θ is the angle between the orbital plane and the kick.

The orbit acquires a new semimajor axis a' from the supernova kick, which is given by

$$a' = \left[\frac{1}{a} \left(2 - \tilde{m} \left(1 + 2\tilde{v} \cos \phi \cos \theta + \tilde{v}^2 \right) \right) \right]^{-1}. \quad (2.4)$$

[Chaurasia & Bailes \(2005\)](#) explore the implications of binary orbits acquiring eccentricity as a result of supernova kicks, finding that $\sim 6\%$ of bound binaries will coalesce $\sim 10^4$ times faster than unperturbed circular binaries. [Figure 2.2](#) shows the eccentricity of the orbit after a supernova kick which is constrained to the orbital plane ($\theta = 0$), plotted in radial-tangential velocity space. Importantly, the area of the low valued eccentricity regions is comparatively tiny, where a disruption to the binary that adds a radial velocity component will introduce significant eccentricity to the orbit.

While these binaries may acquire significant eccentricities from the supernova kick, these DNS circularise from the emission of gravitational waves as they age, and may have negligible eccentricities when they merge as a result (as we will see in [Section 3.2](#)).

2.3 Merger Rates

The formation rate of dynamic DNS is comparatively low to the isolated binary channel. [Bae et al. \(2014\)](#) performed N-body simulations of BBH and DNS binaries formed in globulars, determining

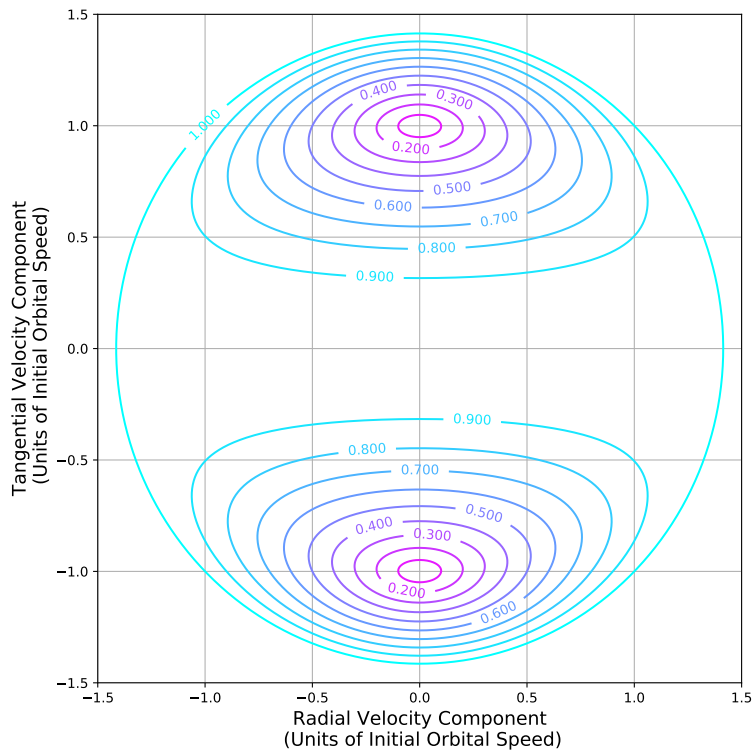


Figure 2.2: Contour map of orbital eccentricity in radial-tangential velocity space. A kick to an initially circular binary ($0, \pm 1$) would likely introduce a significant radial velocity component that gives the binary an eccentric orbit. The boundary of velocity magnitude $\sqrt{2}$ represents the escape velocity, whereafter $e > 1$. Reproduced from [Chaurasia & Bailes \(2005\)](#).

merger rates of 2.5 and 0.27 in each globular cluster per Gyr, respectively. From this they determined a dynamic DNS merger detection rate of 0.0024 yr^{-1} at Advanced LIGO/Virgo. This detection rate is much higher for globular BBH mergers at 15 yr^{-1} , which can be explained by the effect black holes have on inhibiting dynamical DNS formation (see Section 2.1). DNS mergers are predicted to produce short gamma-ray-bursts (GRB), and based on numerical simulations, $\sim 10 - 30\%$ of short-GRBs originating from globular clusters may originate from these mergers ([Grindlay et al., 2006](#)). In their numerical simulations, [Grindlay et al. \(2006\)](#) found a Galactic globular DNS merger rate of 0.04 Myr^{-1} , though they highlighted large uncertainty due to unknowns about production rates and GRB beaming angles. Dynamically formed binaries surrounding supermassive black holes were shown by [Antonini & Perets \(2012\)](#) to have significant eccentricities, with $\sim 10\%$ of these DNS have eccentricities of $e > 0.1$ at 10 Hz. However they found the merger rates for these binaries to be as little as ~ 1 per 10 Myr per Milky-Way-like galaxy.

To evaluate the merger rate of isolated evolution binaries, [Chruslinska et al. \(2017\)](#) employed population synthesis to investigate 21 isolated binary evolution models, finding that only three are consistent with current observational constraints. These three models require either the application of simultaneous changes in the treatment of common envelope such as angular momentum loss and supernova kick behaviour, or the models require a significant increase in the occurrence of core collapse supernovae that allow for DNS to form from small supernova kicks. Interestingly, when calculating the merger rates for BBH under the same models, each rate exceeds that of the observational limits. [Chruslinska et al. \(2017\)](#) believe that this may suggest that the common envelope in DNS evolution may be fundamentally different to the common envelope in BBH formation, or that the supernova kick magnitudes for black hole kicks are greater than DNS kicks.

Performing N-body simulations, [Belczynski et al. \(2018\)](#) find that the isolated evolution channel provides a DNS merger rate $\gtrsim 100$ times that of the dynamical formation channel. They find that the combined merger rate of isolated binary ($10 \text{ Gpc}^{-3} \text{ yr}^{-1}$) and dynamic ($5 \times 10^{-2} \text{ Gpc}^{-3} \text{ yr}^{-1}$) channels is incomparable to the inferred merger rate from GW170817 of $800_{-680}^{+1970} \text{ Gpc}^{-3} \text{ yr}^{-1}$ (revised in [Abbott](#)

et al. (2019)); whereas the combined merger rates for simulated BBH can reproduce the inferred BBH gravitational wave merger rate. Previously it was thought that GW170817 may have been a statistical coincidence, though now with GW190425 being the second NS-NS merger detection this is unlikely and its discovery has provided an increased merger rate of $1090_{-800}^{+1720} \text{ Gpc}^{-3} \text{ yr}^{-1}$ (The LSC and Virgo, 2019; Belczynski et al., 2018).

The local ($z \approx 0$) DNS merger rate calculated by Chruslinska et al. (2017) is ~ 5 times greater than the rate calculated by Belczynski et al. (2018) at $48 \text{ Gpc}^{-3} \text{ yr}^{-1}$. Both are in tension with the observational merger rates found at Advanced LIGO/Virgo. Conversely, Mapelli & Giacobbo (2018) performed numerical simulations using MOBSE, that found they are able to reproduce observational DNS and BBH merger rates by assuming low magnitude core collapse supernova kicks $\sigma \approx 15 \text{ km s}^{-1}$ and a high efficiency of energy transfer during common envelope.

Based on the small contribution the dynamical channel has on the DNS merger rate, it is unlikely that GW190425 formed via this channel, but not impossible.

2.4 GW190425

Fitting a single Gaussian distribution to the total mass of the 10 Galactic DNS that are expected to merge in a Hubble time, we arrive at a mean of $2.69 M_{\odot}$ and standard deviation of $0.12 M_{\odot}$ (see Farrow et al. (2019) and references therein). The inferred total mass of GW190425 is $3.4_{-0.1}^{+0.3} M_{\odot}$, and hence is inconsistent with the observed merging Galactic DNS at a 5σ level, potentially indicating a new population of DNS (The LSC and Virgo, 2019). While the mass of GW190425 is inconsistent with observed Galactic DNS systems, the component masses are consistent with the overall population of neutron stars, where the maximum cutoff mass for a neutron star has been shown to be $2.0_{-0.1}^{+0.1} M_{\odot} \leq M_{\text{NS}} \leq 2.6_{-0.1}^{+0.1} M_{\odot}$ at 90% confidence (Alsing et al., 2018). For GW190425, the larger neutron star mass was recovered at $1.61 - 2.47 M_{\odot}$ and the secondary neutron star mass $1.14 - 1.68 M_{\odot}$ (The LSC and Virgo, 2019).

Here we propose that GW190425 may have formed as an isolated binary via unstable case BB mass transfer, as described in Section 2.2.1. Müller et al. (2016) find that a $\sim 4 - 5 M_{\odot}$ helium star ($\sim 3 M_{\odot}$ CO core) corresponds to a $\sim 2 M_{\odot}$ NS, appropriate for the larger NS of GW190425. Based on this He-NS mass relationship, as well as the inferred GW190425 masses, we propose that the first common envelope left a binary comprised of a $\sim 1.4 M_{\odot}$ neutron star and a $\sim 4 - 5 M_{\odot}$ helium star with an orbital period of $0.1 - 2$ days (Ivanova et al., 2003). Before the CO core of the helium star began to burn, the helium star expanded and overflowed its Roche Lobe, initiating the unstable case BB mass transfer.

During the second common envelope, $\sim 0.05 - 0.1 M_{\odot}$ of mass may have been accreted onto the first born neutron star (MacLeod & Ramirez-Ruiz, 2014). The surviving binary is thought to have an orbital period < 1 hr, making it likely to survive the supernova kick from the second born neutron star. The supernova ejected $\sim 1 M_{\odot}$ leaving a $\sim (1.4 + 2.0) M_{\odot}$ DNS, likely with significant eccentricity.

This short orbital period also makes the DNS difficult to detect in current radio pulsar surveys due to severe Doppler smearing (Cameron et al., 2018; Kyutoku et al., 2018), as well as a short inspiral time of $\lesssim 10$ Myr which makes them unlikely to be detected before they merge compared to other long-lived DNS which have orbital periods of hours to days (see Table 1 of Farrow et al. (2019)).

Chapter 3

Method

We present the method for inferring higher order modes in gravitational wave inference, and apply it towards measuring the eccentricity of GW190425. Then we simulate unstable case BB mass transfer DNS with parameters based on the inferred values of GW190425, as well as those in the literature. We determine the eccentricity of each simulated binary after the supernova kick, and play them forward to 10 Hz. This allows for a comparison between the posterior distribution on the eccentricity of GW190425, and the eccentricities that are expected from unstable case BB mass transfer DNS.

3.1 Searching for Eccentricity in GW190425

We follow the methodology of [Romero-Shaw et al. \(2019\)](#) to recover an eccentric posterior for the parameters GW190425. To avoid performing a computationally expensive analysis of the gravitational wave signal, this recently developed method makes use of likelihood reweighting for including higher order modes in gravitational wave inference ([Payne et al., 2019](#)), such as the inclusion of eccentricity. The outline of the method is as follows: first, perform fiducial Bayesian inference on the GW190425 interferometer data to recover a posterior of leading order parameters, then reweight the inferred posterior samples using the computationally expensive eccentric waveform.

3.1.1 Fiducial Inference

Bilby, a Bayesian inference library for gravitational-wave astronomy ([Ashton et al., 2019](#)), is used to perform fiducial inference using the `IMRPhenomPv2` waveform model ([Khan et al., 2016](#); [Hannam et al., 2014](#)). Source estimation of a gravitational wave inspiral involves a large number of parameters, $(m_1, m_2, d_L, \text{ra}, \text{dec}, \iota, \psi, \phi_c, a_1, a_2, \theta_1, \theta_2, \delta\phi, \phi_{\text{JL}}) \in \Lambda$. The parameters intrinsic to the binary are defined as follows: $m_{1,2}$ are the component masses of the binary, $a_{1,2}$ are the dimensionless spin magnitudes of each star, $\theta_{1,2}$ are the tilt angles between the spin vector and the orbital angular momentum, $\delta\phi$ is the azimuthal angle separating the spin vectors, ϕ_{JL} defines the cone of precession about the system's angular momentum. The extrinsic parameters: d_L is the luminosity distance, ra is the right ascension angle, dec is the declination angle, ι is the angle of inclination between the observer's line of sight and the binary's orbital angular momentum, ψ is the polarisation angle, and ϕ_c is the phase at coalescence.

At low frequencies while the Newtonian approximation of the binary is valid (see, e.g. Section 4.4 of [Abbott et al. \(2016\)](#)), the evolution of the gravitational wave inspiral is characterized by the chirp mass

$$\mathcal{M}_c = \frac{(m_1 m_2)^{3/5}}{(m_1 + m_2)^{1/5}} \quad (3.1)$$

which is generally sampled along with the mass ratio $q = m_1/m_2$, rather than sampling in m_1 and m_2 themselves.

Bilby facilitates *nested sampling*, allowing us to infer a fiducial posterior distribution $p_\theta(\Lambda|D)$ on binary parameters Λ from a gravitational wave signal D . According to Bayes theorem this posterior distribution is given by

Parameter	Prior	Minimum	Maximum
\mathcal{M}_c	uniform	1.420	2.602
$q = m_1/m_2$	uniform	0.125	1
d_L	comoving	1	500
dec	cosine	$-\pi/2$	$\pi/2$
ra	uniform	0	2π
ι (θ_{jn})	sine	0	π
ψ	uniform	0	π
ϕ_c	uniform	0	2π
$\chi_{1,2}$	uniform	-0.8	0.8

Table 3.1: The priors used to infer parameters from GW190425. These values are specific to the IMRPhenomPv2 ROQ basis.

$$p_{\emptyset}(\Lambda|D) = \frac{\mathcal{L}_{\emptyset}(D|\Lambda)\pi(\Lambda)}{\mathcal{Z}} \quad (3.2)$$

where $\mathcal{L}_{\emptyset}(D|\Lambda)$ is the likelihood of the fiducial gravitational waveform described by parameters Λ , of describing the Advanced LIGO/Virgo interferometer data D . The prior distribution $\pi(\Lambda)$ for the parameters Λ is shown in Table 3.1. \mathcal{Z} is the Bayes evidence which acts as a normalisation factor, but can also be used in model selection (Thrane & Talbot, 2019).

The nested sampling procedure is as follows: first, generate a set of N points in parameter space Λ from the prior distribution $\pi(\Lambda)$, then evaluate the likelihood of each point and find the point Λ_k with the lowest likelihood \mathcal{L}^* (Skilling, 2006; Feroz et al., 2009). Next, draw an ellipsoid in parameter space that encapsulates a region of higher likelihood $\mathcal{L} > \mathcal{L}^*$ and sample a new point within this region to replace Λ_k . This process is repeated and the discarded points comprise the posterior. See Feroz et al. (2009) for a complete description of the modern nested sampling algorithm `MultiNest`.

IMRPhenomPv2 is an aligned spin waveform model, meaning that we do not sample for many of the spin angle parameters, and rather sample in dimensionless spin magnitudes $\chi_{1,2}$ (see Lange et al. (2018)). It also includes an effective spin precession parameter χ_p , which we elect to set to zero as this higher order mode changes the waveform only very slightly and no evidence for precession was found for GW190425 (The LSC and Virgo, 2019). As DNS inspiral waveforms are relatively long compared to BBH waveforms, we use a *reduced order quadrature* (ROQ) likelihood that reduces the dimensions of the waveform model whenever applicable, resulting in an increase of computational speed by ~ 70 times (Canizares et al., 2015; Smith et al., 2016). A consequence of using this ROQ likelihood is that it is only applicable for a specific prior, shown in Table 3.1.

3.1.2 Reweighting with Eccentricity

We now seek to reweight our fiducial posterior samples using `SEOBNRE`, an eccentric gravitational waveform model (Cao & Han, 2017). `SEOBNRE` is a spinning effective-one-body-numerical-relativity model for eccentric binaries that can create waveforms with eccentricities $0 \leq e \leq 0.2$. As `SEOBNRE` waveforms can be slow to generate, we elect to use a minimum frequency of 20 Hz rather than 10 Hz, greatly reducing the time duration of the waveform (see Chapter 1.1), and hence decrease waveform generation time by ~ 6 times to ~ 100 s. Despite using shorter waveforms, no information is lost as Advanced LIGO/Virgo’s working minimum frequency is around 20 Hz (Martynov et al., 2016). However, an unfortunate consequence is that the `SEOBNRE` eccentricity values are now cited at a reference frequency of 20 Hz rather than the conventional 10 Hz; as a remedy we use Equation 1.2 to play back the eccentricity to 10 Hz.

We obtain the reweighted posterior using an eccentricity-marginalised `SEOBNRE` likelihood $\mathcal{L}(D|\Lambda)$

$$p(\Lambda|D) = \frac{\mathcal{L}(D|\Lambda)}{\mathcal{L}_{\emptyset}(D|\Lambda)} p_{\emptyset}(\Lambda|D) = w(D|\lambda) p_{\emptyset}(\Lambda|D) \quad (3.3)$$

where the weight for the k th sample is defined as

$$w_k(D|\Lambda_k) = \frac{\mathcal{L}(D|\Lambda_k)}{\mathcal{L}_{\emptyset}(D|\Lambda_k)} \quad (3.4)$$

Reweightings has the effect of reducing the effective number of samples (Wiegand, 1968)

$$n_{\text{eff}} = \frac{(\sum_k w_k)^2}{\sum_k w_k^2} \quad (3.5)$$

from which we calculate a *sampling efficiency* n_{eff}/n , where n is the total number of samples.

Following Romero-Shaw et al. (2019), to obtain this eccentricity-marginalised SEOBNRE likelihood, as well as a one-dimensional eccentricity posterior, we first create a grid of eccentricities log-uniformly distributed between 10^{-6} and 10^{-1} , which acts as our prior on eccentricity. At 10 Hz this prior corresponds to a log-uniform eccentricity distribution $10^{-5.68} \leq e \leq 0.197$.

For each fiducial posterior sample, at each eccentricity bin we create an eccentric SEOBNRE waveform and numerically find the optimal time and phase corresponding to maximum overlap between the fiducial waveform and this newly generated eccentric waveform (see Equation 7 in Payne et al. (2019)). Once in position of maximum overlap, we evaluate the likelihood of the eccentric waveform against the gravitational-wave data.

We take the new likelihood for each eccentricity bin and construct a cumulative likelihood function $\text{CLF}(e)$ with eccentricity as the varying parameter, shown in the bottom of Figure 3.1. From the CLF distribution we can randomly draw a new eccentricity. First we generate a random number x uniformly distributed between $\text{CLF}(e_{\text{min}})$ and $\text{CLF}(e_{\text{max}}) = 1$, and then find the first eccentricity bin k such that $x \geq \text{CLF}(e_k)$, effectively drawing an eccentricity bin from the distribution. Next we uniformly draw an eccentricity from within that bin between e_k and e_{k+1} . We then pair this randomly drawn eccentricity with the other sample parameters to form an eccentric posterior.

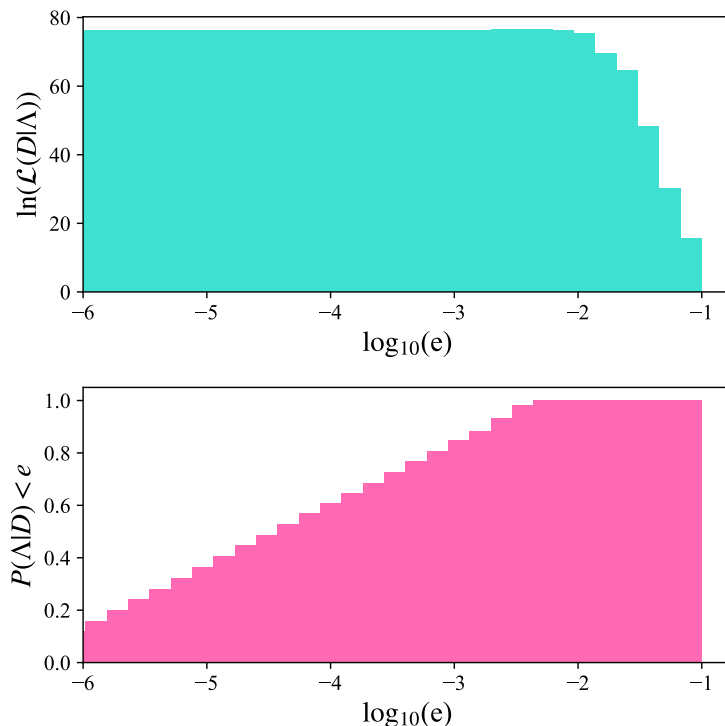


Figure 3.1: Reweighting example for a single posterior sample with parameters Λ . Top: log-likelihoods of eccentric waveforms $\ln(\mathcal{L}(D|\Lambda))$. Bottom: the cumulative likelihood function (CLF), $p(\Lambda|D) < e$.

The average of the eccentric likelihoods is taken for the eccentricity-marginalised likelihood

$$\mathcal{L}_e = \int de \mathcal{L}(d|e) \quad (3.6)$$

from which we can calculate a Bayes factor

$$\mathcal{B} = \frac{\mathcal{L}_e}{\mathcal{L}_\emptyset} \quad (3.7)$$

where \mathcal{L}_\emptyset is the circular evidence $\mathcal{L}(D|e = 0)$. This Bayes factor allows us to evaluate the hypothesis that GW190425 has an eccentricity $e > 0$ against being a circular waveform $e = 0$. A result of $\log \mathcal{B} > 8$ would indicate strong evidence that the waveform is eccentric (Jeffreys, 1961).

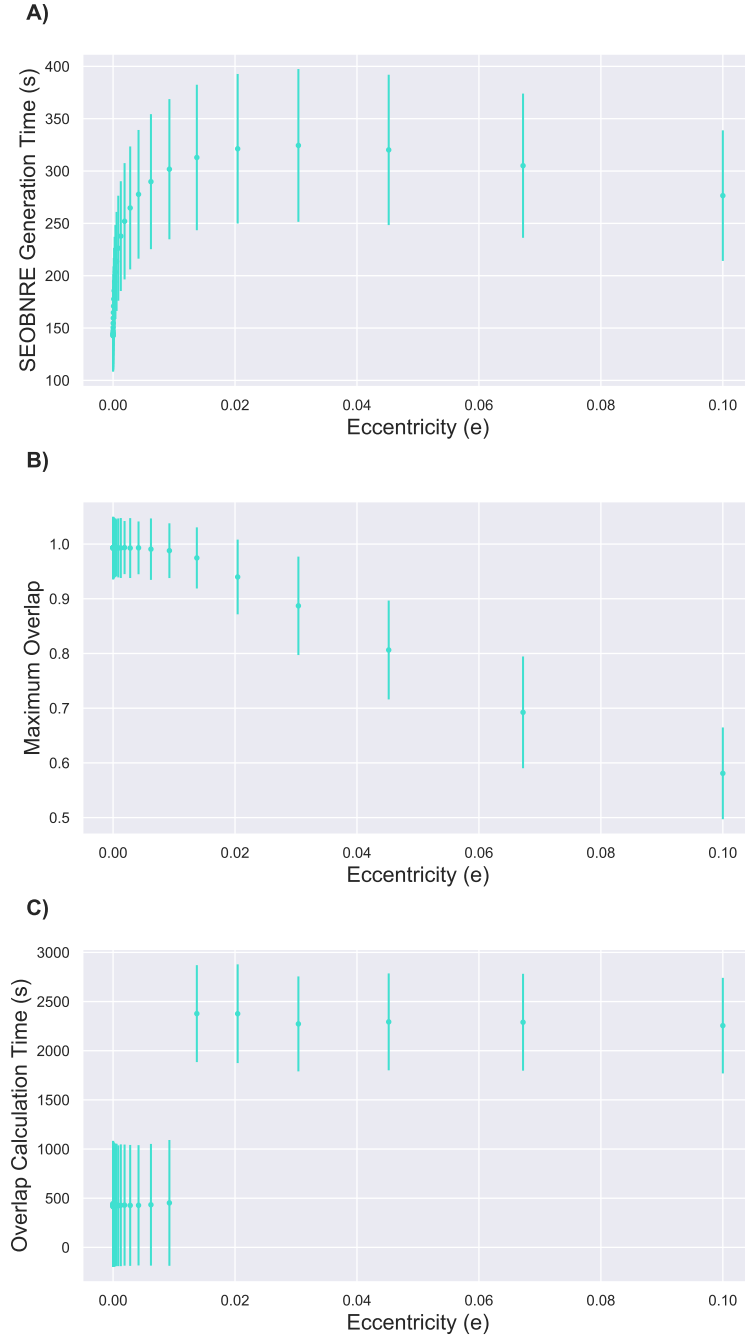


Figure 3.2: A) SEOBNRE waveform generation times, B) Maximum overlap, C) Overlap calculation time. Mean of all 2×10^4 reweighted samples, plotted against eccentricity. Error bars are one standard deviation.

Fortunately, each fiducial posterior sample can be reweighted independently and hence the reweighting can be conducted in parallel. This is most useful as several stages of the reweighting process can be computationally intensive. In particular, the overlap calculation for highly eccentric waveforms ($e > 0.1$) is especially costly as these waveforms may differ significantly from the fiducial waveform, leading to low maximum overlap values as seen in Panel B of Figure 3.2. As our overlap code returns once it reaches an overlap > 0.99 or after 20 attempts, it takes longer to maximise these highly eccentric waveforms as they tend to conclude after 20 attempts rather than the standard $\sim 1 - 8$ attempts. This was alleviated by constraining eccentricity bins to lower eccentricities, by decreasing the maximum eccentricity bin from 0.2 to 0.1, significantly lowering the number of costly overlap evaluations. Reducing the maximum number of overlap maximisation attempts from 20 to 10 also assisted, this was deemed to be a safe choice as overlap values were found to plateau after ~ 8 attempts. This plateau can be seen in Figure 3.2 Panel C, where the time taken for overlap calculations are short for small eccentricities $e \lesssim 0.01$ as the overlap is maximised to > 0.99 after the first attempt; more eccentric waveforms take ~ 8 attempts. As mentioned previously, another computationally expensive component is the generation of the SEOBNRE waveforms for each eccentricity bin (Panel A in Figure 3.2), which we remedied by generating the waveforms from 20 Hz rather than 10 Hz.

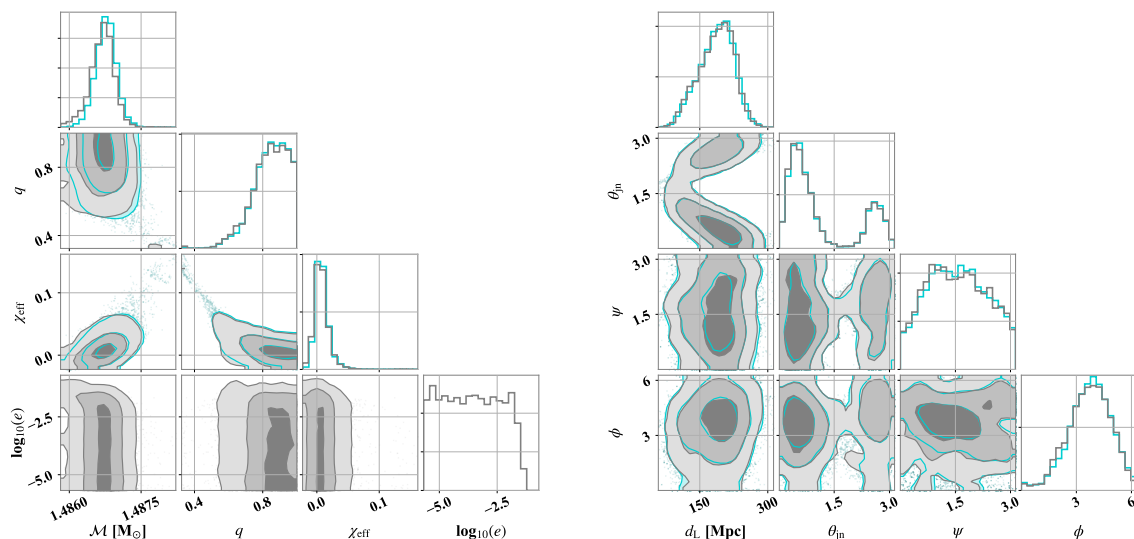


Figure 3.3: Fiducial (turquoise) and reweighted (grey) posterior distributions for GW190425. Intrinsic parameters chirp mass \mathcal{M} , mass ratio q , effective aligned spin χ_{eff} , and log eccentricity $\log_{10}(e)$ are plotted on the left. Extrinsic parameters luminosity distance d_L , binary inclination angle θ_{jn} , polarisation angle ψ , and orbital phase ϕ are plotted on the right.

The eccentricity is played back to 10 Hz using Equation 1.1, and the fiducial and reweighted posteriors are shown in Figure 3.1.2. Our fiducial posterior is in agreement with the [The LSC and Virgo \(2019\)](#) GW190425 discovery paper. An initial reweighting run was conducted on 3×10^3 fiducial samples to evaluate the sampling efficiency. Once this sampling efficiency was deemed sufficient to acquire a reasonably sized effective number of samples, 2×10^4 fiducial samples were reweighted to achieve 7718 effective samples, giving a final reweighting efficiency of 38.6%. The posterior probability distribution for eccentricity resembles our log-uniform prior with $e \lesssim 0.2$, implying we are unable to resolve eccentricities in this low range. We find a Bayes factor of $\mathcal{B} = 0.87$, indicating the data provides no significant support for or against an eccentric waveform. However we are able to constrain the eccentricity of GW190425 to be $e \leq 0.007$ at 10 Hz with 90% confidence.

3.2 Supernova-induced Eccentricity Distribution

Following the proposed formation scenario for GW190425 in Section 2.4, we simulate binaries with $m_1^{(\text{CO})} = 3.0M_\odot$, $m_1^{(\text{NS})} = 2.0M_\odot$, $m_2^{(\text{NS})} = 1.4M_\odot$, with a log-uniform orbital period distribution

between 0.1hr and 1hr at time of supernova as shown in the bottom right panel of Figure 3.4 (See Figure A.1 in Appendix, from Vigna-Gómez et al. (2018)).

Though GW190425 likely experienced a USSN to form the final neutron star, for completeness we simulate both large and small supernovae kicks. Kick velocities are drawn from Maxwellian velocity distributions, shown in the top right of Figure 3.4; with $\sigma_v = 265 \text{ km s}^{-1}$ for large supernova kicks and $\sigma_v = 30 \text{ km s}^{-1}$ for small supernova kicks (see Section 2.2.2). We simulate isotropic kicks with no preference for any particular direction. The resulting orbital eccentricity is calculated with Equation 2.3 (Figure 3.4 left panel), and new semimajor axis with Equation 2.4 which is converted into an orbital period using Kepler’s third law (Figure 3.4 bottom right panel). Some neutron stars receive kicks sufficient to disrupt the binary with $e \geq 1$, and hence are discarded. All binaries survive the small-kick supernovae, whereas only 90.3% of binaries survive the larger kick velocities. This can be seen in the left panel of Figure 3.4, where the large kick eccentricity distribution extends all the way up to $e = 1$. We also see that the large supernovae kicks create eccentric binaries that span the entire domain $0 < e < 1$, compared to tight range of eccentricities caused by smaller kicks $0.2 \lesssim e \lesssim 0.4$.

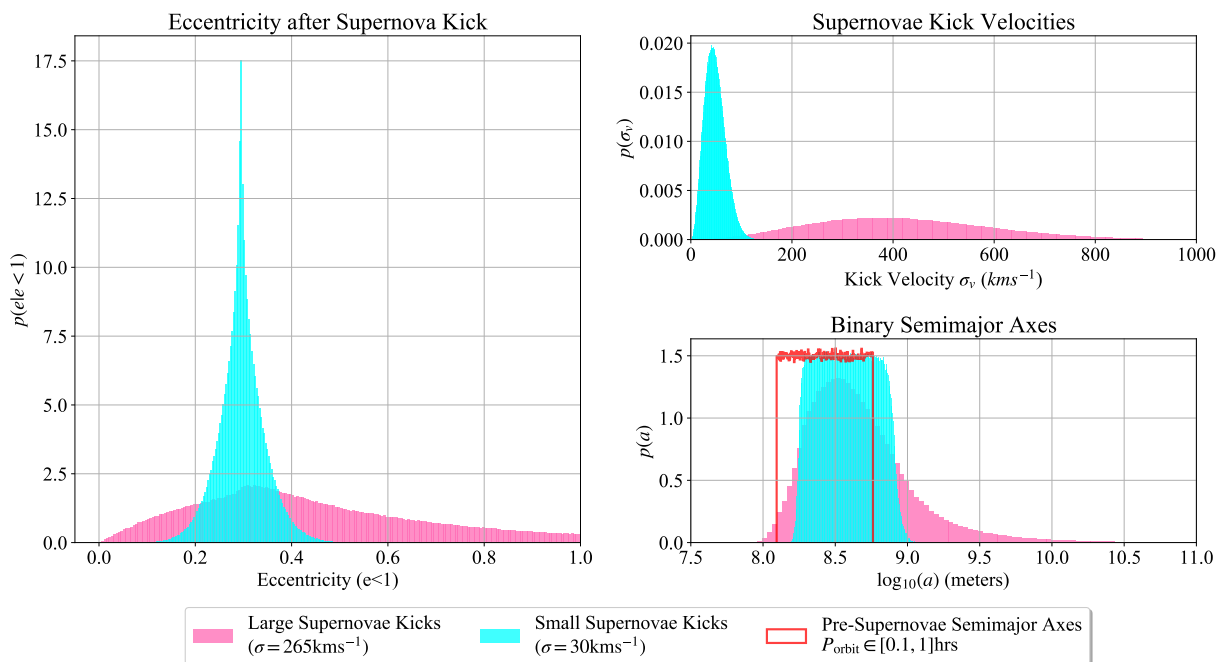


Figure 3.4: Top Right: Maxwell-Boltzmann kick velocity distributions for large kicks (265 km s^{-1}) in pink, small kicks (30 km s^{-1}) in blue. Bottom Right: Semimajor axes distributions before and after supernovae for simulated DNS; initial log-uniform semimajor axis distribution shown by red line. Left: Eccentricity distributions immediately after supernovae.

Each surviving simulated binary is then evolved with Equation 1.2 to a period of 0.2 s, corresponding to a gravitational-wave frequency of $f_{\text{gw}} = 10 \text{ Hz}$. The eccentricity distributions for large and small supernova kicks are presented in Figure 3.5, compared against the recovered GW190425 eccentricity posterior from Section 3.1. The eccentricity from small kick velocities spans $10^{-4.94} \leq e \leq 10^{-3.98}$, and for large kick velocities $10^{-4.89} \leq e \leq 10^{-3.79}$, both at 90% confidence. The larger supernovae kick velocities result in slightly higher eccentricities with a mean of $10^{-4.30}$ compared to the small-kick mean of $10^{-4.46}$.

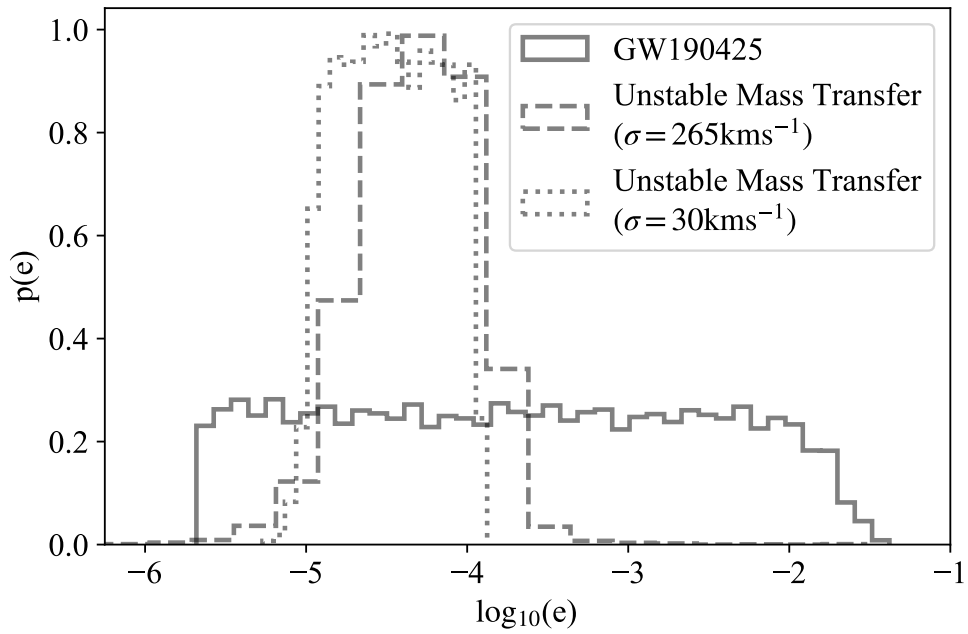


Figure 3.5: Simulated eccentricity distributions for large (dashed) and small (dotted) kick velocity distributions under binary assumptions for GW190425; compared to the recovered eccentricity distribution from GW190425. All distributions are shown at a mean gravitational wave frequency of 10 Hz.

Chapter 4

Discussion

4.1 GW190425 & Simulated Eccentricity Distributions

In Figure 3.5, the eccentricity of GW190425 is consistent with the simulated unstable case BB mass transfer binary eccentricities. However it is not currently possible for us to resolve these small eccentricities at 10 Hz with our second generation gravitational wave detectors. The flat GW190425 eccentricity distributions in log-space (Figure 3.1.2 & Figure 3.5) closely resemble our log-uniform prior, though we can see that support for eccentricities $e \gtrsim 10^{-2}$ begins to drop off. Waveforms with eccentricities beyond this value become increasingly dissimilar to the GW190425 signal, and thus we have been able to constrain the eccentricity of the event to $e \leq 0.007$ with 90% confidence. No support is found for GW190425 having an eccentricity $e > 0.04$. We have not ruled out the possibility that GW190425 formed via dynamical formation as this channel can also lead to circular binaries ($e \approx 0$), nonetheless we have proposed an alternate formation history as an unstable case BB mass transfer binary, that avoids the ill-matched dynamical merger rate.

Interestingly the dashed histogram line for large-kick simulated DNS in Figure 3.5 extends far past the 90% confidence region, up to $e = 0.029$. These rare outliers resulted from some DNS receiving an extremely large ($\approx 1000 \text{ km s}^{-1}$) retrograde ($\phi \approx \pi$) supernova kick within the orbital plane ($\theta \approx 0$), giving the star an almost parabolic eccentricity $e \approx 0.9$ in a near-capture orbit which only slightly decays before emitting gravitational waves at 10 Hz (Bate et al., 1971).

In our simulations it has been assumed that supernovae kicks are isotropic. Constraining the angle of the kick, such as within the orbital plane ($\theta \approx 0$), results in slightly different eccentricity distributions post-supernova. Though, our results at 10 Hz were found to be robust against such a choice.

It is not surprising that GW190425, and the revisited GWTC-1 events by Romero-Shaw et al. (2019), have eccentricities consistent with zero. Significant eccentricities at 10 Hz are only expected to arise from binaries formed via the dynamic channel, and only a small fraction ($\sim 5\%$) of dynamic BBH are expected to have $e \geq 0.1$ (Rodriguez et al., 2018b,a), and likely an even smaller fraction for DNS due to neutron stars being prevented from effectively participating in these exchange interactions (Banerjee, 2017b). The comparative merger rates between isolated evolution and dynamical formation DNS makes an eccentric DNS gravitational wave detection even less likely.

Furthermore, the current waveforms in the Advanced LIGO/Virgo detection pipeline do not include eccentricity. The current quasi-circular models are only effective for detecting slightly eccentric waveforms $e < 0.1$, albeit with a lower signal-to-noise ratio than a non-eccentric waveform (Brown & Zimmerman, 2010; Lower et al., 2018).

4.2 Future Eccentric Waveform Models

Complete inspiral-merger-ringdown eccentric waveform models that are computationally efficient may soon be available, such as ENIGMA which is comprised of an eccentric inspiral matched with a machine-learning trained quasi-circular merger appropriate for $e \lesssim 0.2$ (Huerta et al., 2018). Tiwari et al. (2019) have also recently developed an analytic post-Newtonian eccentric waveform model for moderately ec-

centric inspirals, $e \leq 0.15$ for DNS. Incorporation of these models into the Advanced LIGO/Virgo detection pipeline may allow for direct detection of eccentric events and inference of eccentric posteriors.

4.3 Future Detection

The future third generation of gravitational wave detectors, such as the Einstein Telescope (Sathyaprakash et al., 2011) and Cosmic Explorer (Abbott et al., 2017), will be able to observe gravitational waves at higher signal-to-noise ratios and with improved low-frequency sensitivity. Other detectors, such as the space-based Laser Interferometer Space Antenna (LISA) will extend gravitational wave observation down to the mHz regime (Amaro-Seoane et al., 2017), with a minimum design frequency 10^{-4} Hz. Figure 4.1 shows the simulated unstable case BB mass transfer DNS eccentricities at 5×10^{-4} Hz, which exhibit wide eccentricity distributions for large and small supernova kicks. At these low frequencies it will be possible to observe the orbital eccentricity encoded in the gravitational waves of DNS that form via unstable case BB mass transfer, and those which form through other isolated or dynamic formation channels (Breivik et al., 2016; Nishizawa et al., 2016). Given enough observations, we may be able to use population statistics with eccentricity to probe the contributions of different formation channels to the total population of merging DNS.

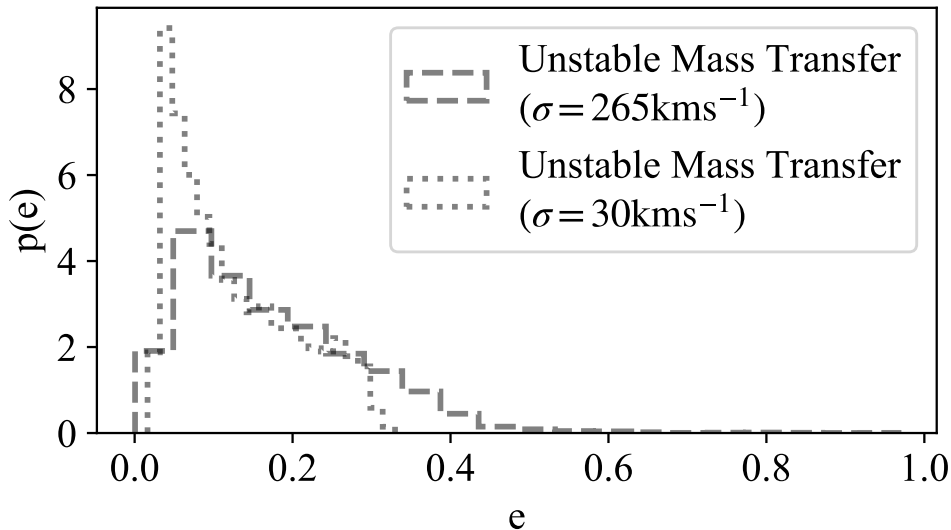


Figure 4.1: Simulated eccentricity distributions for large (dashed) and small (dotted) kick velocity distributions at 5 mHz, which will be within the frequency band of future detector LISA.

Along with the improved sensitivity of these detectors will come new challenges, such as the problem of detecting gravitational waves from potentially millions of sources at once. In contrast to Advanced LIGO/Virgo, data from LISA will be populated mostly with gravitational wave signals rather than instrumental noise (Vallisneri, 2009). Many of the LISA sources are long-lived where it will be able to detect binaries with orbital periods as large as $P_{\text{orbit}} \leq \frac{2}{10^{-4}\text{Hz}} \approx 5.5\text{Hr}$. As LISA revolves around the Sun, the long gravitational wave signals will be Doppler shifted, imprinting information of sky location into the signals (Amaro-Seoane et al., 2017). While this may make distinguishing sources easier, it also has the additional effect of introducing more intrinsic parameters of sky position and orientation, which will be necessary parameters for waveform models. Advanced LIGO/Virgo currently uses a template bank of waveforms which span the parameter space m_1 and m_2 to search for gravitational waves. However for LISA this kind of search will likely be infeasible due to the added dimensionality, which makes such a template bank impractical. For higher order waveforms, such as those which include eccentricity, will also have to adapt to this increased dimensionality while still endeavouring to remain computationally efficient.

Another challenge is the ability to generate long-duration high-order waveforms which we have already seen difficulty with using **SEOBNRE**. LISA will be able to detect a population of pre-inspiral circular binaries that will have simpler waveform models due to their negligible frequency evolution. Eccentric binaries such as unstable case BB mass transfer DNS, may be particularly hard to model as they will have long waveforms as well as appreciable change in frequency as the binary circularises.

Chapter 5

Conclusion

The formation of the progenitor of GW190425 may have involved an unstable case BB mass transfer. Using Bayesian reweighting methods we have constrained the eccentricity of GW190425 at 10 Hz to be $e \leq 0.007$ with 90% confidence. With a Bayes factor of $\mathcal{B} = 0.87$ we find no significant support for or against GW190425 being eccentric. The simulated unstable case BB mass transfer DNS, which we based on the inferred parameters of GW190425 and literature, have broad ranges of eccentricity after their final supernova kicks. After playing these simulated DNS forward to 10 Hz we compared the dampened eccentricity distributions to the recovered eccentricity distribution of GW190425. However we are currently unable to resolve the small residual eccentricity of this event and thus are unable to determine whether the eccentricity of GW190425 matches the simulated unstable case BB binaries. Being the second DNS merger detection, if GW190425 indeed formed through unstable case BB mass transfer then it may be possible that roughly half of merging DNS form via this channel. Future detectors such as space-based LISA will have heightened sensitivity at low frequencies and may be able to use measurements of eccentricity to distinguish between DNS populations and their respective formation scenarios.

Appendix A

Appendix

We can derive Equation 1.2 by first noting that the gravitational wave frequency is twice that of the binary frequency, i.e. $f_{\text{GW}} = 2f_{\text{orbit}} = \frac{2}{P_{\text{orbit}}}$ due to the quadrupolar nature of gravitational waves.

Then we can substitute $P_{\text{orbit}} = \frac{2}{f_{\text{GW}}}$ into Kepler's third law

$$a = \left(\frac{\mu P^2}{4\pi^2} \right)^{1/3} = \left(\frac{\mu \left(\frac{2}{f_{\text{GW}}} \right)^2}{4\pi^2} \right)^{1/3} = \left(\frac{\mu}{\pi^2 f_{\text{GW}}^2} \right)^{1/3} \quad (\text{A.1})$$

where $\mu = G(M_1 + M_2)$. Next we can use Equation A.1 find the ratio of two gravitational wave frequencies f and f_0 in terms of their semimajor axes a and a_0

$$\frac{f}{f_0} = \left(\frac{\mu}{\pi^2 a^3} \right)^{1/2} / \left(\frac{\mu}{\pi^2 a_0^3} \right)^{1/2} = \left(\frac{a_0}{a} \right)^{3/2} \quad (\text{A.2})$$

From here we can substitute in Equation 1.1 for each semimajor axis, giving Equation 1.2

$$\frac{f(e)}{f_0(e_0)} = \left(\frac{\beta(e_0)}{\beta(e)} \right)^{3/2} \quad \text{where } \beta(e) = \frac{e^{12/19}}{(1-e^2)} \left[1 + \frac{121}{304} e^2 \right]^{\frac{870}{2299}} \quad (\text{A.3})$$

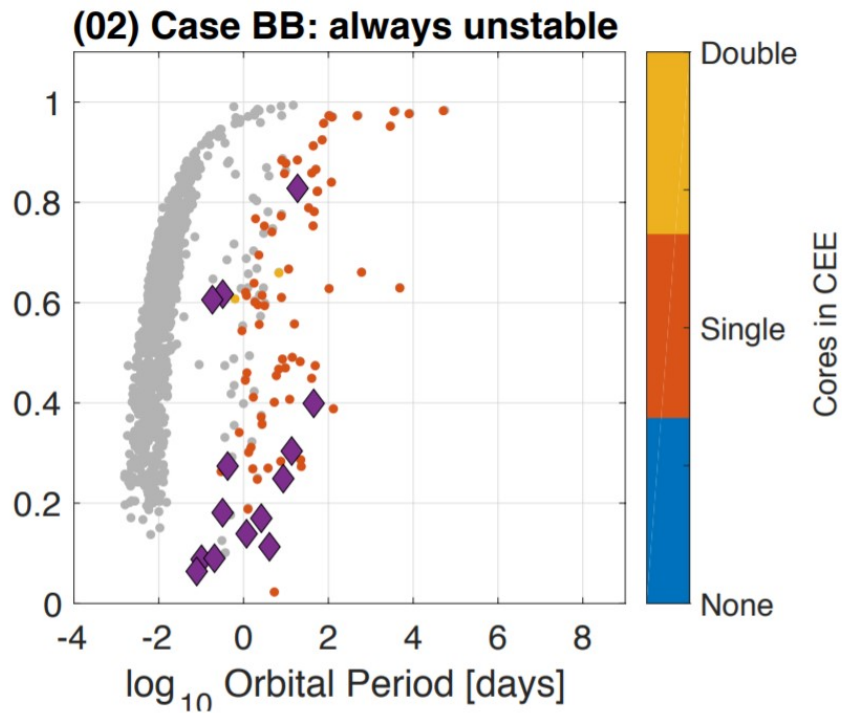


Figure A.1: The \log_{10} orbital periods of unstable case BB mass transfer DNS as simulated by [Vigna-Gómez et al. \(2018\)](#) (Figure 8) using COMPAS. The periods are approximately log-uniformly distributed between 0.1–1 hr. Purple diamonds represent Galactic DNS. Color denotes the number of cores within the common envelope phase: orange for a double-core common envelope, red for a single core, and blue for no cores.

References

- Abbott, B., Abbott, R., Abbott, T., et al. 2019, *Physical Review X*, 9, doi: [10.1103/physrevx.9.031040](https://doi.org/10.1103/physrevx.9.031040)
- Abbott, B. P., Abbott, R., Abbott, T. D., et al. 2016, *Annalen der Physik*, 529, 1600209, doi: [10.1002/andp.201600209](https://doi.org/10.1002/andp.201600209)
- Abbott, B. P., et al. 2017, *Classical and Quantum Gravity*, 34, 044001, doi: [10.1088/1361-6382/aa51f4](https://doi.org/10.1088/1361-6382/aa51f4)
- Alsing, J., Silva, H. O., & Berti, E. 2018, *Monthly Notices of the Royal Astronomical Society*, 478, 1377, doi: [10.1093/mnras/sty1065](https://doi.org/10.1093/mnras/sty1065)
- Amaro-Seoane, P., Audley, H., Babak, S., et al. 2017, arXiv e-prints, arXiv:1702.00786. <https://arxiv.org/abs/1702.00786>
- Antonini, F., & Perets, H. B. 2012, *The Astrophysical Journal*, 757, 27, doi: [10.1088/0004-637x/757/1/27](https://doi.org/10.1088/0004-637x/757/1/27)
- Antonini, F., Toonen, S., & Hamers, A. S. 2017, *The Astrophysical Journal*, 841, 77, doi: [10.3847/1538-4357/aa6f5e](https://doi.org/10.3847/1538-4357/aa6f5e)
- Ashton, G., Hübner, M., Lasky, P. D., et al. 2019, *The Astrophysical Journal Supplement Series*, 241, 27, doi: [10.3847/1538-4365/ab06fc](https://doi.org/10.3847/1538-4365/ab06fc)
- Bae, Y.-B., Kim, C., & Lee, H. M. 2014, *Monthly Notices of the Royal Astronomical Society*, 440, 2714, doi: [10.1093/mnras/stu381](https://doi.org/10.1093/mnras/stu381)
- Banerjee, S. 2017a, *Monthly Notices of the Royal Astronomical Society*, 467, 524, doi: [10.1093/mnras/stw3392](https://doi.org/10.1093/mnras/stw3392)
- . 2017b, *Monthly Notices of the Royal Astronomical Society*, 473, 909, doi: [10.1093/mnras/stx2347](https://doi.org/10.1093/mnras/stx2347)
- Bate, R., Mueller, D., & White, J. 1971, *Fundamentals of Astrodynamics*, Dover Books on Aeronautical Engineering Series (Dover Publications). <https://books.google.com.au/books?id=UtJK8cetqGkC>
- Belczynski, K., Kalogera, V., & Bulik, T. 2002, *The Astrophysical Journal*, 572, 407, doi: [10.1086/340304](https://doi.org/10.1086/340304)
- Belczynski, K., Askar, A., Arca-Sedda, M., et al. 2018, *A&A*, 615, A91, doi: [10.1051/0004-6361/201732428](https://doi.org/10.1051/0004-6361/201732428)
- Beniamini, P., & Piran, T. 2016, *Monthly Notices of the Royal Astronomical Society*, 456, 4089, doi: [10.1093/mnras/stv2903](https://doi.org/10.1093/mnras/stv2903)
- Boss, A. P. 1988, *Comments on Astrophysics*, 12, 169
- Brandt, N., & Podsiadlowski, P. 1995, *Monthly Notices of the Royal Astronomical Society*, 274, 461, doi: [10.1093/mnras/274.2.461](https://doi.org/10.1093/mnras/274.2.461)

- Breivik, K., Rodriguez, C. L., Larson, S. L., Kalogera, V., & Rasio, F. A. 2016, *The Astrophysical Journal*, 830, L18, doi: [10.3847/2041-8205/830/1/118](https://doi.org/10.3847/2041-8205/830/1/118)
- Brown, D. A., & Zimmerman, P. J. 2010, *Physical Review D*, 81, 024007, doi: [10.1103/PhysRevD.81.024007](https://doi.org/10.1103/PhysRevD.81.024007)
- Cameron, A. D., Champion, D. J., Kramer, M., et al. 2018, *Monthly Notices of the Royal Astronomical Society: Letters*, 475, L57, doi: [10.1093/mnrasl/sly003](https://doi.org/10.1093/mnrasl/sly003)
- Canizares, P., Field, S. E., Gair, J., et al. 2015, *Physical Review Letters*, 114, doi: [10.1103/physrevlett.114.071104](https://doi.org/10.1103/physrevlett.114.071104)
- Cao, Z., & Han, W.-B. 2017, *Physical Review D*, 96, 044028, doi: [10.1103/PhysRevD.96.044028](https://doi.org/10.1103/PhysRevD.96.044028)
- Chaurasia, H. K., & Bailes, M. 2005, *The Astrophysical Journal*, 632, 1054, doi: [10.1086/444447](https://doi.org/10.1086/444447)
- Chruslinska, M., Belczynski, K., Klencki, J., & Benacquista, M. 2017, *Monthly Notices of the Royal Astronomical Society*, 474, 2937–2958, doi: [10.1093/mnras/stx2923](https://doi.org/10.1093/mnras/stx2923)
- Delgado, A. J., & Thomas, H. C. 1981, *Astronomy & Astrophysics*, 96, 142
- Dewi, J. D. M., & Pols, O. R. 2003, *Monthly Notices of the Royal Astronomical Society*, 344, 629, doi: [10.1046/j.1365-8711.2003.06844.x](https://doi.org/10.1046/j.1365-8711.2003.06844.x)
- Dewi, J. D. M., Pols, O. R., Savonije, G. J., & van den Heuvel, E. P. J. 2002, *Monthly Notices of the Royal Astronomical Society*, 331, 1027, doi: [10.1046/j.1365-8711.2002.05257.x](https://doi.org/10.1046/j.1365-8711.2002.05257.x)
- Farrow, N., Zhu, X.-J., & Thrane, E. 2019, *Astrophysical Journal*, 876, 18, doi: [10.3847/1538-4357/ab12e3](https://doi.org/10.3847/1538-4357/ab12e3)
- Feroz, F., Hobson, M. P., & Bridges, M. 2009, *Monthly Notices of the Royal Astronomical Society*, 398, 1601, doi: [10.1111/j.1365-2966.2009.14548.x](https://doi.org/10.1111/j.1365-2966.2009.14548.x)
- Finzi, A., & Wolf, R. A. 1967, *APJ*, 150, 115, doi: [10.1086/149317](https://doi.org/10.1086/149317)
- Grindlay, J., Zwart, S. P., & McMillan, S. 2006, *Nature Physics*, 2, 116, doi: [10.1038/nphys214](https://doi.org/10.1038/nphys214)
- Gunn, J. E., & Ostriker, J. P. 1970, *The Astrophysical Journal*, 160, 979, doi: [10.1086/150487](https://doi.org/10.1086/150487)
- Hannam, M., Schmidt, P., Bohé, A., et al. 2014, *Physical Review Letters*, 113, 151101, doi: [10.1103/PhysRevLett.113.151101](https://doi.org/10.1103/PhysRevLett.113.151101)
- Hansen, B. M. S., & Phinney, E. S. 1997, *Monthly Notices of the Royal Astronomical Society*, 291, 569, doi: [10.1093/mnras/291.3.569](https://doi.org/10.1093/mnras/291.3.569)
- Hobbs, G., Lorimer, D. R., Lyne, A. G., & Kramer, M. 2005, *Monthly Notices of the Royal Astronomical Society*, 360, 974, doi: [10.1111/j.1365-2966.2005.09087.x](https://doi.org/10.1111/j.1365-2966.2005.09087.x)
- Huerta, E. A., Moore, C. J., Kumar, P., et al. 2018, *Physical Review D*, 97, 024031, doi: [10.1103/PhysRevD.97.024031](https://doi.org/10.1103/PhysRevD.97.024031)
- Ivanova, N., Belczynski, K., Kalogera, V., Rasio, F. A., & Taam, R. E. 2003, *The Astrophysical Journal*, 592, 475, doi: [10.1086/375578](https://doi.org/10.1086/375578)
- Jeffreys, H. 1961, *Theory of probability*, 3rd edn. (Oxford, England: Oxford University Press)
- Khan, S., Husa, S., Hannam, M., et al. 2016, *Physical Review D*, 93, doi: [10.1103/physrevd.93.044007](https://doi.org/10.1103/physrevd.93.044007)
- Kozai, Y. 1962, *Astronomical Journal*, 67, 591, doi: [10.1086/108790](https://doi.org/10.1086/108790)

- Kyutoku, K., Nishino, Y., & Seto, N. 2018, *Monthly Notices of the Royal Astronomical Society*, 483, 2615–2620, doi: [10.1093/mnras/sty3322](https://doi.org/10.1093/mnras/sty3322)
- Lange, J., O’Shaughnessy, R., & Rizzo, M. 2018. <https://arxiv.org/abs/1805.10457>
- Lidov, M. L. 1962, *Planetary and Space Science*, 9, 719, doi: [10.1016/0032-0633\(62\)90129-0](https://doi.org/10.1016/0032-0633(62)90129-0)
- Lower, M. E., Thrane, E., Lasky, P. D., & Smith, R. 2018, *Physical Review D*, 98, 083028, doi: [10.1103/PhysRevD.98.083028](https://doi.org/10.1103/PhysRevD.98.083028)
- MacLeod, M., & Ramirez-Ruiz, E. 2014, *The Astrophysical Journal*, 798, L19, doi: [10.1088/2041-8205/798/1/119](https://doi.org/10.1088/2041-8205/798/1/119)
- Mandel, I., & Farmer, A. 2018. <https://arxiv.org/abs/1806.05820>
- Mapelli, M., & Giacobbo, N. 2018, *Monthly Notices of the Royal Astronomical Society*, 479, 4391, doi: [10.1093/mnras/sty1613](https://doi.org/10.1093/mnras/sty1613)
- Martynov, D., Hall, E., Abbott, B., et al. 2016, *Physical Review D*, 93, doi: [10.1103/physrevd.93.112004](https://doi.org/10.1103/physrevd.93.112004)
- Michaely, E., Ginzburg, D., & Perets, H. B. 2016. <https://arxiv.org/abs/1610.00593>
- Müller, B., Heger, A., Liptai, D., & Cameron, J. B. 2016, *Monthly Notices of the Royal Astronomical Society*, 460, 742, doi: [10.1093/mnras/stw1083](https://doi.org/10.1093/mnras/stw1083)
- Nishizawa, A., Sesana, A., Berti, E., & Klein, A. 2016, *Monthly Notices of the Royal Astronomical Society*, 465, 4375, doi: [10.1093/mnras/stw2993](https://doi.org/10.1093/mnras/stw2993)
- O’Leary, R. M., Kocsis, B., & Loeb, A. 2009, *Monthly Notices of the Royal Astronomical Society*, 395, 2127, doi: [10.1111/j.1365-2966.2009.14653.x](https://doi.org/10.1111/j.1365-2966.2009.14653.x)
- Paczynski, B. 1976, in *IAU Symposium, Vol. 73, Structure and Evolution of Close Binary Systems*, ed. P. Eggleton, S. Mitton, & J. Whelan, 75
- Payne, E., Talbot, C., & Thrane, E. 2019, arXiv e-prints, arXiv:1905.05477. <https://arxiv.org/abs/1905.05477>
- Peters, P. C. 1964, *Physical Review*, 136, B1224, doi: [10.1103/PhysRev.136.B1224](https://doi.org/10.1103/PhysRev.136.B1224)
- Pfahl, E., Rappaport, S., & Podsiadlowski, P. 2002, *The Astrophysical Journal*, 571, L37, doi: [10.1086/341197](https://doi.org/10.1086/341197)
- Podsiadlowski, P., Langer, N., Poelarends, A. J. T., et al. 2004, *The Astrophysical Journal*, 612, 1044, doi: [10.1086/421713](https://doi.org/10.1086/421713)
- Rakavy, G., Shaviv, G., & Zinamon, Z. 1967, *APJ*, 150, 131, doi: [10.1086/149318](https://doi.org/10.1086/149318)
- Rodriguez, C. L., Amaro-Seoane, P., Chatterjee, S., et al. 2018a, *Physical Review D*, 98, 123005, doi: [10.1103/PhysRevD.98.123005](https://doi.org/10.1103/PhysRevD.98.123005)
- Rodriguez, C. L., Amaro-Seoane, P., Chatterjee, S., & Rasio, F. A. 2018b, *Physical Review Letters*, 120, 151101, doi: [10.1103/PhysRevLett.120.151101](https://doi.org/10.1103/PhysRevLett.120.151101)
- Rodriguez, C. L., Zevin, M., Pankow, C., Kalogera, V., & Rasio, F. A. 2016, *The Astrophysical Journal*, 832, L2, doi: [10.3847/2041-8205/832/1/12](https://doi.org/10.3847/2041-8205/832/1/12)
- Romero-Shaw, I. M., Lasky, P. D., & Thrane, E. 2019. <https://arxiv.org/abs/1909.05466>
- Samsing, J., D’Orazio, D. J., Kremer, K., Rodriguez, C. L., & Askar, A. 2019. <https://arxiv.org/abs/1907.11231>

- Sathyaprakash, B., Abernathy, M., Acernese, F., et al. 2011. <https://arxiv.org/abs/1108.1423>
- Schwab, J., Podsiadlowski, P., & Rappaport, S. 2010, *The Astrophysical Journal*, 719, 722, doi: [10.1088/0004-637x/719/1/722](https://doi.org/10.1088/0004-637x/719/1/722)
- Sigurdsson, S., & Hernquist, L. 1993, *Nature*, 364, 423, doi: [10.1038/364423a0](https://doi.org/10.1038/364423a0)
- Skilling, J. 2006, *Bayesian Analysis*, 1, 833, doi: [10.1214/06-BA127](https://doi.org/10.1214/06-BA127)
- Smith, R., Field, S. E., Blackburn, K., et al. 2016, *Physical Review D*, 94, doi: [10.1103/physrevd.94.044031](https://doi.org/10.1103/physrevd.94.044031)
- Sparks, W. M., & Stecher, T. P. 1974, *ApJ*, 188, 149, doi: [10.1086/152697](https://doi.org/10.1086/152697)
- Stevenson, S., Berry, C. P. L., & Mandel, I. 2017, *Monthly Notices of the Royal Astronomical Society*, 471, 2801, doi: [10.1093/mnras/stx1764](https://doi.org/10.1093/mnras/stx1764)
- Stevenson, S., Ohme, F., & Fairhurst, S. 2015, *The Astrophysical Journal*, 810, 58, doi: [10.1088/0004-637x/810/1/58](https://doi.org/10.1088/0004-637x/810/1/58)
- Stovall, K., Freire, P. C. C., Chatterjee, S., et al. 2018, *Astrophysical Journal Letters*, 854, L22, doi: [10.3847/2041-8213/aaad06](https://doi.org/10.3847/2041-8213/aaad06)
- Tauris, T. M., Langer, N., Moriya, T. J., et al. 2013, *The Astrophysical Journal*, 778, L23, doi: [10.1088/2041-8205/778/2/L23](https://doi.org/10.1088/2041-8205/778/2/L23)
- Tauris, T. M., Langer, N., & Podsiadlowski, P. 2015, *Monthly Notices of the Royal Astronomical Society*, 451, 2123, doi: [10.1093/mnras/stv990](https://doi.org/10.1093/mnras/stv990)
- Tauris, T. M., Kramer, M., Freire, P. C. C., et al. 2017, *The Astrophysical Journal*, 846, 170, doi: [10.3847/1538-4357/aa7e89](https://doi.org/10.3847/1538-4357/aa7e89)
- The LSC and Virgo. 2019, In preparation
- The LSC and Virgo, & Salemi, F. 2019. <https://arxiv.org/abs/1907.09384>
- Thrane, E., & Talbot, C. 2019, *Publications of the Astronomical Society of Australia*, 36, doi: [10.1017/pasa.2019.2](https://doi.org/10.1017/pasa.2019.2)
- Tiwari, S., Gopakumar, A., Haney, M., & Hemantakumar, P. 2019, *Physical Review D*, 99, 124008, doi: [10.1103/PhysRevD.99.124008](https://doi.org/10.1103/PhysRevD.99.124008)
- Vallisneri, M. 2009, *Classical and Quantum Gravity*, 26, 094024, doi: [10.1088/0264-9381/26/9/094024](https://doi.org/10.1088/0264-9381/26/9/094024)
- Vigna-Gómez, A., Neijssel, C. J., Stevenson, S., et al. 2018, *Monthly Notices of the Royal Astronomical Society*, 481, 4009–4029, doi: [10.1093/mnras/sty2463](https://doi.org/10.1093/mnras/sty2463)
- Wiegand, H. 1968, *Biometrische Zeitschrift*, 10, 88, doi: [10.1002/bimj.19680100122](https://doi.org/10.1002/bimj.19680100122)
- Zevin, M., Kremer, K., Siegel, D. M., et al. 2019. <https://arxiv.org/abs/1906.11299>
- Zhu, X., Thrane, E., Osłowski, S., Levin, Y., & Lasky, P. D. 2018, *Physical Review D*, 98, 043002, doi: [10.1103/PhysRevD.98.043002](https://doi.org/10.1103/PhysRevD.98.043002)
- Zwart, S. F. P., & McMillan, S. L. W. 2000, *The Astrophysical Journal*, 528, L17, doi: [10.1086/312422](https://doi.org/10.1086/312422)